Journal of Medical Imaging

MedicalImaging.SPIEDigitalLibrary.org

Construction of realistic phantoms from patient images and a commercial three-dimensional printer

Shuai Leng
Baiyu Chen
Thomas Vrieze
Joel Kuhlmann
Lifeng Yu
Amy Alexander
Jane Matsumoto
Jonathan Morris
Cynthia H. McCollough

SPIE.

Shuai Leng, Baiyu Chen, Thomas Vrieze, Joel Kuhlmann, Lifeng Yu, Amy Alexander, Jane Matsumoto, Jonathan Morris, Cynthia H. McCollough, "Construction of realistic phantoms from patient images and a commercial three-dimensional printer," *J. Med. Imag.* **3**(3), 033501 (2016), doi: 10.1117/1.JMI.3.3.033501.

Construction of realistic phantoms from patient images and a commercial three-dimensional printer

Shuai Leng,[a,*] Baiyu Chen,[a] Thomas Vrieze,[a] Joel Kuhlmann,[b] Lifeng Yu,[a] Amy Alexander,[a] Jane Matsumoto,[a] Jonathan Morris,[a] and Cynthia H. McCollough[a]
[a]Mayo Clinic, Department of Radiology, 200 First Street SW, Rochester, Minnesota 55905, United States
[b]Mayo Clinic, Division of Engineering, 200 First Street SW, Rochester, Minnesota 55905, United States

Abstract. The purpose of this study was to use three-dimensional (3-D) printing techniques to construct liver and brain phantoms having realistic pathologies, anatomic structures, and heterogeneous backgrounds. Patient liver and head computed tomography (CT) images were segmented into tissue, vessels, liver lesion, white and gray matter, and cerebrospinal fluid (CSF). Stereolithography files of each object were created and imported into a commercial 3-D printer. Printing materials were assigned to each object after test scans, which showed that the printing materials had CT numbers ranging from 70 to 121 HU at 120 kV. Printed phantoms were scanned on a CT scanner and images were evaluated. CT images of the liver phantom had measured CT numbers of 77.8 and 96.6 HU for the lesion and background, and 137.5 to 428.4 HU for the vessels channels, which were filled with iodine solutions. The difference in CT numbers between lesions and background (18.8 HU) was representative of the low-contrast values needed for optimization tasks. The liver phantom background was evaluated with Haralick features and showed similar texture between patient and phantom images. CT images of the brain phantom had CT numbers of 125, 134, and 108 HU for white matter, gray matter, and CSF, respectively. The CT number differences were similar to those in patient images. [DOI: 10.1117/1.JMI.3.3.033501]

Keywords: phantom; liver; brain; three-dimensional printer; computed tomography; image quality.

Paper 16043R received Mar. 11, 2016; accepted for publication Jun. 16, 2016; published online Jul. 7, 2016.

1 Introduction

Subsequent to concerns on increased radiation dose from computed tomography (CT) imaging, a large collection of dose reduction methods have been investigated, such as automatic exposure control, optimized tube potential (kV) selection, projection, or image-based denoising techniques, and iterative reconstruction (IR) algorithms.[1–10] To follow the "as low as reasonably achievable" (ALARA) principle, the lowest radiation dose that can be used without sacrificing diagnostic performance should be used. To address the question, "how low can we go," an objective assessment of image quality is needed. This is particularly important for IR and denoising techniques that involve nonlinear processes. Conventional image quality metrics, such as modulation transfer function, noise power spectrum, and contrast-to-noise ratio may not be sufficient to evaluate image quality in these scenarios. For example, recent studies reported degraded low-contrast detectability using IR and decreased radiation doses, although conventional image quality is still maintained.[11–13] Task-based image quality metrics based on model observers have gained popularity in CT image quality evaluation, especially for application in image-quality assessment of IR algorithms.[14–20] Several previous studies have demonstrated a good correlation between the performance of human observer and model observer.[17–19,21–23] Most of these studies were performed using phantoms with uniform background due to simplicity and availability of these phantoms. However, to assess image quality and radiation dose reduction in clinical CT imaging, physical phantoms having realistic background textures and lesions are highly desirable as the performance of reconstruction algorithms may be affected by anatomic background (i.e., structured noise).[24]

Although some anthropomorphic phantoms are commercially available, they usually represent generic patients rather than individual patients. The background is usually homogeneous and phantoms are difficult to customize. Therefore, there is an unmet need to construct patient-specific phantoms with realistic background structures. Additive manufacturing, or three-dimensional (3-D) printing, has been widely used in industry and recently its application in medicine has been explored.[25–31] Compared to conventional phantom manufacturing, 3-D printing techniques have the advantage of constructing complex physical objects in a shorter time and with less effort. This flexibility enables fast construction of patient-specific models for individualized medicine. Therefore, the purpose of this study was to three dimensionally print a realistic liver phantom with a metastatic lesion and a realistic brain phantom with an acute cerebral infarction, which could be used for image-quality assessment, radiation dose reduction, and other research and educational activities.

2 Methods and Materials

The 3-D printer (Objet Connex350, Stratasys, MN) used in this study is based on the PolyJet 3-D printing technique, which is similar to inkjet printing but with layers of curable liquid photopolymers being deposited onto a tray to build smooth and detailed 3-D models. The general procedure of 3-D printing

*Address all correspondence to: Shuai Leng, E-mail: leng.shuai@mayo.edu

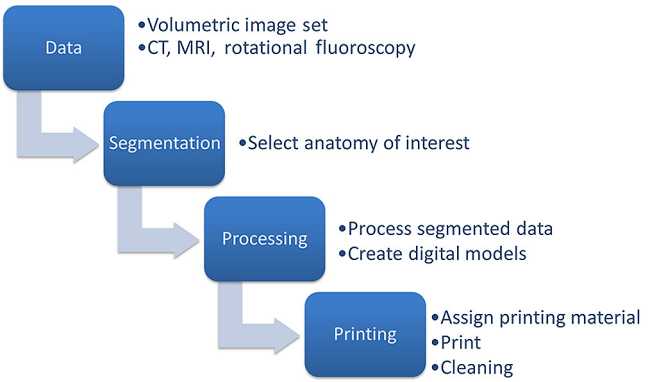

Fig. 1 Flowchart of the 3-D printing procedure.

can be summarized in four major steps, as shown in the following flowchart (Fig. 1). The whole process is reproducible given that the same procedures (as mentioned below) are used for segmentation, the same software is used for processing, and the same 3-D printer is used for printing.

1. Data acquisition: 3-D printing starts with volumetric image data. For the liver phantom, patient images from a contrast-enhanced liver CT scan with a metastatic lesion were used. The patient was scanned on a 128-slice scanner (Definition Flash, Siemens Healthcare, Forchheim, Germany) with 100 kV and 445 effective mAs. The corresponding volume CT dose index ($CTDI_{vol}$) was 18 mGy. The images were reconstructed using a medium sharp kernel (B40) at 3-mm slice thickness. For the brain phantom, images of a patient with an acute cerebral infarction were chosen. The patient was scanned on the same 128-slice scanner model as previously mentioned, but with 120 kV and 250 effective mAs. The corresponding $CTDI_{vol}$ was 38 mGy. The images were reconstructed using a medium sharp kernel (J40) at 2-mm slice thickness.

2. Segmentation: the second step in 3-D printing is to segment images into anatomy of interest. Patient images were loaded into commercial software (Mimics, Materialise, Belgium) for segmentation. For the liver phantom, the images were segmented into several objects, inducing liver tissues, a liver lesion, and liver vessels. The segmentation was performed mainly based on a CT number threshold, with additional procedures such as region growing, morphology operations, and multislice editing (applying the manual editing done on one slice to other slices, using interpolation if necessary). To reflect the heterogeneity of liver background (liver parenchyma with varying linear attenuation coefficients), liver tissues were thresholded into two groups of roughly equal volume. Only two groups are used in our case because the selection of materials with proper x-ray attenuation was limited (as shown in Section 3). For the brain phantom, the images were segmented similarly into three objects, including white matter, gray matter, and cerebrospinal fluid (CSF). The pathology of interest (hypoattenuation of the lentiform nucleus due to acute stroke) had similar attenuation as white matter, and therefore was combined with white matter.

3. Processing: segmented data were then processed to generate digital models using commercial software (3Matic, Materialise, Belgium). Model editing (referred to as wrapping and fixing) was performed to remove abrupt changes at model boundaries and eliminate bad triangles before outputting the stereolithography (STL) files for each segmented object.

4. Printing: the STL files were then loaded to the 3-D printer to print the phantom. Each segmented object was assigned a specific printing material, which was a mixture of two base printing materials (two cartridges). Note that to construct phantoms that mimic patient anatomy in CT images, materials with appropriate attenuation properties are needed. Therefore, cylindrical rods made from various printing materials were scanned on a CT scanner (Definition Force, Siemens Healthcare) at nine different tube potentials (the most available on a CT scanner), from 70 to 150 kV at 10 kV steps. Based on the measured CT numbers of the materials, appropriate printing materials were assigned to each object in the phantoms. The final selection of printing material for each object is reported in the Results section.

The printed liver phantom was first scanned in air and then placed in a 35-cm × 26-cm oblong-shaped water phantom, which represented the attenuation of the abdomen for a standard size adult patient. The combined phantom (liver and water) was scanned on a 192-slice CT scanner (Definition Force, Siemens Healthcare). Automatic exposure control (CareDose 4D) was turned on with quality reference mAs (QRM) of 80, 120, 160, 240, and 360, which corresponded to $CTDI_{vol}$ of 5.2, 7.7, 10.2, 15.4, and 23.1 mGy. As a reference, the phantom was also scanned at a very high dose level, 147.6 mGy, to show the structures with minimal noise. Images were reconstructed at 3-mm slice thickness and 250-mm field of view, using standard filtered backprojection (FBP) with a medium sharp kernel (Br40). The printed brain phantom was placed

Fig. 2 CT numbers of printing materials at tube potentials from 70 to 150 kV. The materials used for the liver lesion, the heterogeneous liver background, white matter, gray matter, and CSF are annotated.

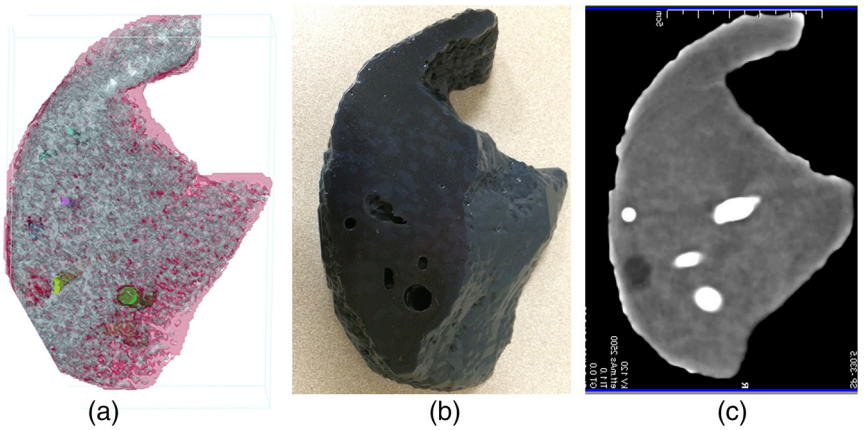

Fig. 3 Segmentation of the (a) liver phantom model, (b) photograph, and (c) CT image of the printed liver phantom. The display window width and window center are 100 and 80 HU. Heterogeneity of the liver tissue can be observed in the CT image.

in a skull phantom. The gap between the brain phantom and the skull was filled with water. The combined phantom (brain and skull) was scanned on the same 192 slice CT scanner using 120 kV and effective mAs of 250, which corresponded to $CTDI_{vol}$ of 35.4 mGy. As a reference, the phantom was also scanned at a very high dose level, 265.6 mGy, to show the structures with minimal noise. Brain images were reconstructed at 2-mm slice thickness and 200-mm field of view, using FBP with a medium sharp kernel (Hr40s).

To quantitatively evaluate the background texture of the liver phantom, 2-cm × 2-cm regions of interest (ROI) were cropped from the liver parenchyma of patient images and liver phantom images (19 ROIs each for patient and phantom images). Haralick texture analysis[32] was performed based on the ROIs, and the texture was compared between the patient images and the liver phantom images in terms of homogeneity, energy, correlation, contrast, and entropy.

3 Results

3.1 *Computed Tomography Numbers for Printing Materials*

The measured CT numbers for available printing materials are shown in Fig. 2. For the same printing material, 70 kV had the lowest CT number while 150 kV had the highest CT number. For the most commonly used tube potential, 120 kV, the CT numbers ranged from 70 to 121 HU. The materials used for printing and their CT numbers at each tube potential are shown in Fig. 2. For the liver phantom, the difference between the printing materials (1 to 51 HU at 120 kV) covered the range of contrast that could potentially be seen between liver tissues and low-contrast liver lesions, but not the range of contrast that could be seen between the enhanced vessels and the liver tissue. Therefore, support material instead of printing material was

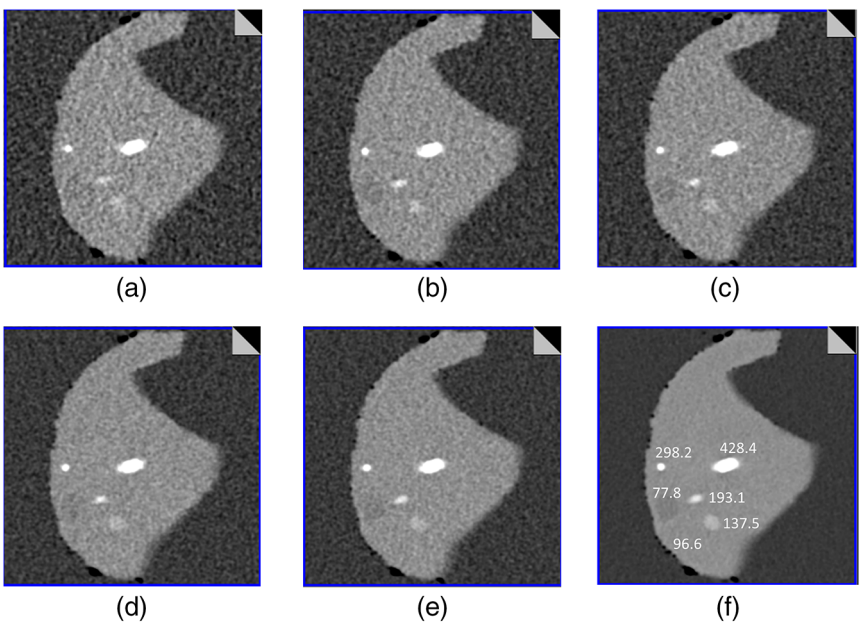

Fig. 4 CT images of the liver phantom scanned at six different dose levels with $CTDI_{vol}$ of (a) 5.2, (b) 7.7, (c) 10.2, (d) 15.4, (e) 23.1, and (f) 147.6 mGy. Measured CT numbers of lesion, tissue, and vessels (in the unit of Hounsfield unit) are marked on (f).

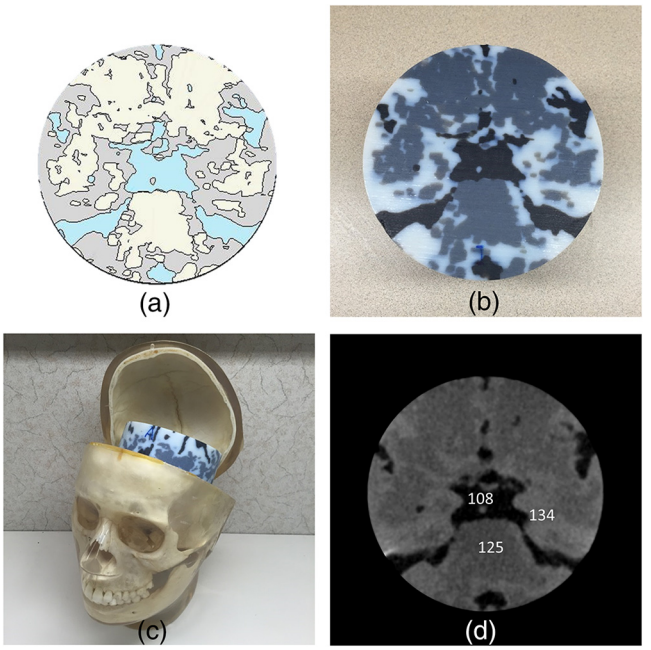

Fig. 5 (a) Segmentation of the brain phantom model, (b) photograph of the printed brain phantom, (c) placement of the brain phantom in a skull phantom, and (d) a CT image of the brain phantom acquired at very high dose, with CT numbers measured in the unit of Hounsfield unit. The display window width and window center for (d) are 80 and 145 HU.

assigned to the vessels. The support material was washed out afterwards, resulting in hollow vessels in the liver phantom. These hollow vessels were then filled with iodine solutions (6, 10, 15, and 20 mgI/ml) and sealed. For the brain phantom, the CT numbers of these printing materials were too high for brain tissue. Therefore, materials that had the same relative CT numbers as brain tissues were chosen (i.e., materials that maintained the contrast between white matter, gray matter, and CSF were chosen).

3.2 *Printed Phantoms*

The printed liver phantom had a size of $13 \times 9.5 \times 2.5$ cm. The production cost was around $100 (the authors' institute owns the 3-D printer so this reflects only the cost of the printing materials). The production time was a few hours. Note that the printed phantom was in the same scale as the real liver, but only the inferior portion of the liver was printed (2.5-cm thick). This was because the purpose of this phantom was not to replicate the entire liver, but to demonstrate that 3-D printing technique can imitate realistic liver background textures. A portion of the liver was sufficient to demonstrate this point, while saving cost and time. The printed brain phantom had a size of $10 \times 10 \times 6$ cm. The production cost was around $300. The production time was a few hours. The printed phantom was in the same scale as the real brain, but only a cylindrical portion (the center of the brain) was printed, so that the phantom could be placed into the skull phantom.

Figure 3(a) shows the segmented liver phantom model. Figure 3(b) shows a photograph of the printed liver phantom, where the two colors on the surface (subtle difference) represent the two background printing materials, and the holes represent the vessels. Figure 3(c) shows a CT image of the physical phantom scanned in air. Variations in the CT numbers of the areas with liver tissues represented the background heterogeneity of liver CT images, which represents patient anatomy better than a uniform background. The low-contrast lesion and high-contrast vessels can all be appreciated from this image. Figure 4 shows the CT images of the liver phantom scanned in the water phantom at six dose levels with $CTDI_{vol}$ of 5.2, 7.7, 10.2, 15.4, 23.1, and 147.6 mGy. All structures including lesion, tissue, and vessels are clearly delineated in the high dose [147.6 mGy, Fig. 4(f)] reference image. The influence of image noise can be observed from images scanned with clinically relevant dose levels [5.2 to 23.1 mGy, Figs. 4(a)–4(e)]. It can be observed from these images that as noise increased with decreased radiation dose, the lesion became less visible. Figure 4(f) also shows the measured CT numbers, which were in the appropriate range of clinically observed CT numbers for contrast-enhanced liver scans. The contrast between the lesion (77.8 HU) and the background (96.6 HU) was 18.8 HU.

Figure 5(a) shows the segmented brain phantom model. Figure 5(b) shows a photograph of the printed brain phantom. Figure 5(c) shows the placement of the brain phantom in the skull phantom. Figure 5(d) shows a slice of the brain phantom image and the CT number measurements. The CT numbers of white matter, gray matter, and CSF were 125, 134, and 108, respectively, which were different from clinically observed brain CT numbers as a result of the limited choice of printing materials. However, the CT number differences between white matter, gray matter, and CSF were similar to those of patient brain CT images. Therefore, when viewed with the same display window width but different window level, the phantom images and the original patient images (the images used for segmentation) showed similar ranges of gray scales and contrast levels, and similarities in anatomical structure (Fig. 6). The

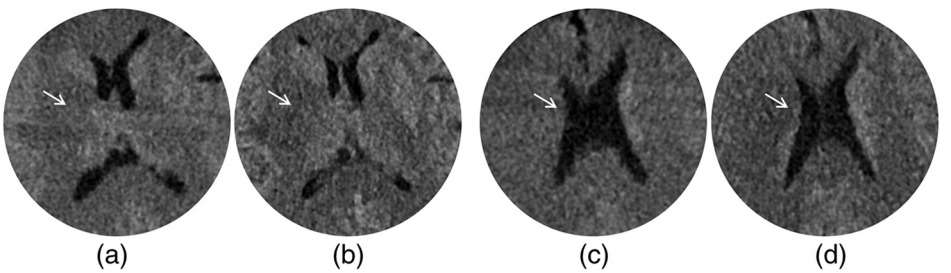

Fig. 6 (a), (c) The images of the brain phantom acquired at clinical dose level compared to (b), (d) the images of the original patient. The hypoattenuation of the lentiform nucleus due to acute stroke is indicated by the arrow. The display window width and window center for (a) and (c) are 80 and 145 HU. The display window width and window center for (b) and (d) are 80 and 40 HU.

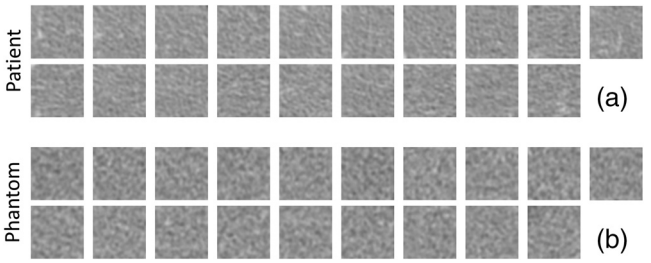

Fig. 7 ROIs cropped from the liver parenchyma of (a) patient images and (b) liver phantom images. The display window width and window center are 400 and 40 HU.

Table 1 Haralick texture feature analysis results.

	Patient images	Phantom images
Homogeneity	0.94 ± 0.01	0.94 ± 0.01
Energy	0.64 ± 0.07	0.41 ± 0.05
Correlation	0.51 ± 0.05	0.57 ± 0.03
Contrast	0.13 ± 0.02	0.19 ± 0.02
Entropy	0.78 ± 0.12	1.12 ± 0.07

hypoattenuation of the lentiform nucleus due to acute stroke can also be appreciated.

3.3 *Texture Analysis*

The 19 ROIs cropped from patient images and the 19 ROIs cropped from liver phantom images are shown in Fig. 7. The quantitative comparison of the ROIs in terms of Haralick texture features are shown in Table 1. In general, the patient images and the phantom images have similar texture. However, the similarity could be further improved if more than two printing materials are used to generate the heterogeneous liver background (if more printing materials with proper x-ray attenuation properties become available).

4 Discussions and Conclusions

Body habitus and anatomical features vary from patient to patient, which needs to be taken into consideration when evaluating CT images. To accommodate this need, this work describes a method to construct patient-specific phantoms with heterogeneous background textures and anatomically realistic structures that were based on patient CT images and created with a commercial 3-D printer. With the proposed method, a patient-specific phantom could be created, which could be used for individualized protocol optimization. In addition, multiple phantoms could be created based on multiple patients' anatomy to present a realistic patient cohort.

Although only two materials were used in this study to create heterogeneous background, more materials could be used if needed. By changing the mixture of the printing material, the degree of heterogeneity can be adjusted to the desired level. The heterogeneous background demonstrated in this work enables investigation of the effect of radiation dose reduction techniques on the detection of subtle liver lesions in a realistic background, instead of in a uniform background, as most previous studies have done. We further demonstrated the change in image quality that occurs with changes in dose in the context of realistic background textures using the printed liver phantom.

The results shown in Fig. 2 provided a look-up table of CT numbers for each material at each tube potential. In addition to the phantoms built in this study, this look-up table could be used in building any other phantoms using these printing materials. Appropriate printing materials can be selected based on this look-up table and the desired CT numbers of the phantom. As shown in Fig. 2, CT numbers of each material depended on the tube potential. The same material had lower CT number at lower tube potentials. This tube potential dependence was similar to fat, but different than for other materials such as iodine or calcium, whose CT number increase with decreasing tube potential. This tube potential dependence needs to be taken into account if phantoms are intended to be used in studies involving different tube potential settings.

Although the 3-D printer used in this study has an in-plane spatial resolution of 0.04 millimeter, CT images usually have an in-plane resolution of only 0.5-1 mm. As a result, only major vessels in the liver were segmented. The small vessels became part of the heterogeneous background, which were mimicked by the two materials.

Liver and brain phantoms were used as an example to demonstrate the procedure of constructing patient-specific phantoms using the 3-D printing techniques. The same procedure could be used to construct phantoms representing other body parts. One challenge of constructing these phantoms is the availability of printing materials that represent the wide range of attenuation properties encountered in CT imaging, such as tissue, bone, and contrast media. This is different from other applications of 3-D printed models, such as those used for surgical planning or guidance, where the requirement is to accurately represent the shape, color, and geometry of the anatomy, not the x-ray attenuation. For the printer investigated, current available materials have attenuation (CT numbers) in the range of soft tissue, potentially limiting its applicability to organs mainly consisting of soft tissue, such as the brain, liver, pancreas, and kidneys. In this study, we used a technique of filling hollow vessels with iodine solutions to mimic highly attenuating vessels. It is also possible to include a "hollow" lesion in the phantom that could be filled with liquids having varying attenuation properties (e.g., varying iodine concentrations), thus being able to target a specific lesion contrast. This method might also be used to represent highly attenuating bony structures, by printing a hollow space for the bony structures and filling with an iodine- or calcium-based solution. The most elegant solution is to have 3-D printer manufacturers develop high-attenuation materials that are compatible with their 3-D printers. This could be achieved by mixing available printing materials with highly attenuating materials, such as iodine, barium, or bismuth. Yoo et al.[28] modified a 3-D printer and mixed iodine contrast with printing power to generate high-attenuating bone-mimicking materials. This, however, is not currently available on commercial 3-D printers.

In conclusion, realistic liver and brain phantoms with heterogeneous backgrounds and realistic pathology were constructed from patient CT images using a commercial 3-D printer. These printed phantoms potentially could be used to determine the effect of radiation dose reduction and noise reduction techniques

on the ability of detecting subtle pathology in the context of realistic background textures.

Acknowledgments

This work was supported by the National Institute of Biomedical Imaging and Bioengineering of the National Institutes of Health under Award Nos. R01 EB017095 and U01 EB017185 and a research grant from Department of Radiology, Mayo Clinic. The authors would like to thank Dr. David DeLone for helping identify the clinical case used in this study. They would also like to thank Ms. Kristina Nunez for her assistance with manuscript preparation. The content is solely the responsibility of the authors and does not necessarily represent the official views of the National Institutes of Health.

References

1. C. McCollough et al., "Achieving routine sub-mSv CT scanning: report from the summit on management of radiation dose in CT," *Radiology* **264**(2), 567–580 (2012).
2. M. K. Kalra et al., "Computed tomography radiation dose optimization: scanning protocols and clinical applications of automatic exposure control," *Curr. Probl. Diagn. Radiol.* **34**(5), 171–181 (2005).
3. C. H. McCollough, M. R. Bruesewitz, and J. M. Kofler Jr., "CT dose reduction and dose management tools: overview of available options," *Radiographics* **26**(2), 503–512 (2006).
4. P. J. La Rivière, J. Bian, and P. A. Vargas, "Penalized-likelihood sinogram restoration for computed tomography," *IEEE Trans. Med. Imaging* **25**(8), 1022–1036 (2006).
5. J. Wang et al., "Penalized weighted least-squares approach to sinogram noise reduction and image reconstruction for low-dose X-ray computed tomography," *IEEE Trans. Med. Imaging* **25**(10), 1272–1283 (2006).
6. A. K. Hara et al., "Iterative reconstruction technique for reducing body radiation dose at CT: feasibility study," *Am. J. Roentgenol.* **193**(3), 764–771 (2009).
7. L. Yu et al., "Automatic selection of tube potential for radiation dose reduction in CT: a general strategy," *Med. Phys.* **37**(1), 234–243 (2010).
8. L. Yu et al., "Radiation dose reduction in computed tomography: techniques and future perspective (PMC3271708)," *Imaging Med.* **1**(1), 65–84 (2009).
9. W. A. Kalender, H. Wolf, and C. Suess, "Dose reduction in CT by anatomically adapted tube current modulation. II. Phantom measurements," *Med. Phys.* **26**(11), 2248–2253 (1999).
10. J. B. Thibault et al., "A three-dimensional statistical approach to improved image quality for multislice helical CT," *Med. Phys.* **34**(11), 4526–4544 (2007).
11. M. E. Baker et al., "Contrast-to-noise ratio and low-contrast object resolution on full- and low-dose MDCT: SAFIRE versus filtered back projection in a low-contrast object phantom and in the liver," *Am. J. Roentgenol.* **199**(1), 8–18 (2012).
12. A. H. Goenka et al., "Effect of reduced radiation exposure and iterative reconstruction on detection of low-contrast low-attenuation lesions in an anthropomorphic liver phantom: an 18-reader study," *Radiology* **272**(1), 154–163 (2014).
13. S. T. Schindera et al., "Iterative reconstruction algorithm for CT: can radiation dose be decreased while low-contrast detectability is preserved?," *Radiology* **269**(2), 511–518 (2013).
14. K. L. Boedeker and M. F. McNitt-Gray, "Application of the noise power spectrum in modern diagnostic MDCT: part II. Noise power spectra and signal to noise," *Phys. Med. Biol.* **52**(14), 4047–4061 (2007).
15. A. Wunderlich and F. Noo, "Image covariance and lesion detectability in direct fan-beam x-ray computed tomography," *Phys. Med. Biol.* **53**(10), 2471–2493 (2008).
16. S. Richard and J. H. Siewerdsen, "Comparison of model and human observer performance for detection and discrimination tasks using dual-energy x-ray images," *Med. Phys.* **35**(11), 5043–5053 (2008).
17. L. Yu et al., "Prediction of human observer performance in a 2-alternative forced choice low-contrast detection task using channelized Hotelling observer: impact of radiation dose and reconstruction algorithms," *Med. Phys.* **40**(4), 041908 (2013).
18. S. Leng et al., "Correlation between model observer and human observer performance in CT imaging when lesion location is uncertain," *Med. Phys.* **40**(8), 081908 (2013).
19. Y. Zhang et al., "Correlation between human and model observer performance for discrimination task in CT," *Phys. Med. Biol.* **59**(13), 3389–3404 (2014).
20. B. Chen et al., "Evaluating iterative reconstruction performance in computed tomography," *Med. Phys.* **41**(12), 121913 (2014).
21. K. Li, J. Garrett, and G.-H. Chen, "Correlation between human observer performance and model observer performance in differential phase contrast CT," *Med. Phys.* **40**(11), 111905 (2013).
22. I. Hernandez-Giron et al., "Comparison between human and model observer performance in low-contrast detection tasks in CT images: application to images reconstructed with filtered back projection and iterative algorithms," *Br. J. Radiol.* **87**(1039), 20140014 (2014).
23. J. Solomon et al., "Diagnostic performance of an advanced modeled iterative reconstruction algorithm for low-contrast detectability with a third-generation dual-source multidetector CT scanner: potential for radiation dose reduction in a multireader study," *Radiology* **275**(3), 142005 (2015).
24. J. Solomon and E. Samei, "Quantum noise properties of CT images with anatomical textured backgrounds across reconstruction algorithms: FBP and SAFIRE," *Med. Phys.* **41**(9), 091908 (2014).
25. J. Matsumoto et al., "Three-dimensional physical modeling: applications and experience at mayo clinic," *Radiographics* **35**(7), 1989–2006 (2015).
26. M. H. Michalski and J. S. Ross, "The shape of things to come: 3D printing in medicine," *JAMA* **312**(21), 2213–2214 (2014).
27. M. A. Miller and G. D. Hutchins, "Development of anatomically realistic PET and PET/CT phantoms with rapid prototyping technology," in *IEEE Nuclear Science Symp. Conf. Record*, Vol. 6, pp. 4252–4257 (2007).
28. T. S. Yoo et al., "Toward quantitative X-ray CT phantoms of metastatic tumors using rapid prototyping technology," in *IEEE Int. Symp. on Biomedical Imaging: From Nano to Macro*, pp. 1770–1773 (2011).
29. J. Solomon, F. Bochud, and E. Samei, "Design of anthropomorphic textured phantoms for CT performance evaluation," *Proc. SPIE* **9033**, 90331U (2014).
30. D. Mitsouras et al., "Medical 3D printing for the radiologist," *Radiographics* **35**(7), 1965–1988 (2015).
31. S. Leng et al., "Construction of realistic liver phantoms from patient images using 3D printer and its application in CT image quality assessment," *Proc. SPIE* **9412**, 94124E (2015).
32. R. M. Haralick, K. Shanmugam, and I. Dinstein, "Textural features for image classification," *IEEE Trans. Syst. Man Cybern.* **SMC–3**(6), 610–621 (1973).

Shuai Leng received his BS degree in engineering physics in 2001, an MS degree in engineering physics in 2003, from Tsinghua University, and his PhD degree in medical physics in 2008 from the University of Wisconsin, Madison. He is an associate professor of medical physics at the Mayo Clinic in Rochester, Minnesota. He has authored over 100 peer-reviewed articles. His research interest is technical development and clinical application of X-ray and CT imaging.

Baiyu Chen received his BS degree in engineering physics in 2008 from Tsinghua University, and his PhD degree in medical physics in 2014 from Duke University. She is a research fellow in the Radiology Department of Mayo Clinic in Rochester, Minnesota. Her research interest is the evaluation and optimization of CT image quality.

Joel Kuhlmann received his BS degree in electrical engineering in 1986, from Case Western Reserve University, and an MS degree in mechanical engineering in 1987, from Rensselaer Polytechnic Institute. He is a principal engineer in the Division of Engineering at the Mayo Clinic in Rochester, Minnesota.

Lifeng Yu received his BS degree in nuclear physics in 1997 and an MEng degree in nuclear technology in 2000, both from Beijing University, and a PhD in medical physics from the University of

Chicago in 2006. He is an associate professor of medical physics at Mayo Clinic. He is the author of over 90 journal articles and holds 10 patents. His research interests include CT physics, image quality assessment, and spectral CT.

Cynthia H. McCollough received her BS degree in physics from Hope College in 1985, an MS degree in medical physics from the University of Wisconsin, Madison, in 1986, and a PhD degree in medical physics from the University of Wisconsin, Madison, in 1991. She is a professor of medical physics and biomedical engineering at the Mayo Clinic in Rochester, Minnesota, where she directs the multidisciplinary CT Clinical Innovation Center.